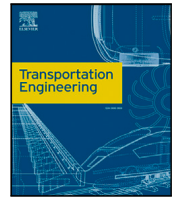# Energy consequences of separating velocity planning and torque distribution in overactuated electric vehicles

(article starts on next page)

Full length article

Energy consequences of separating velocity planning and torque distribution in overactuated electric vehicles

Juliette Torinsson [a,b] [*,1], Mats Jonasson [a], Derong Yang [b], Bengt Jacobson [a], Toheed Ghandriz [a,c]

[a] Chalmers University of Technology, Department of Vehicle Engineering and Autonomous Systems, Göteborg, Sweden
[b] Volvo Car Corporation, Department of Vehicle Motion Control, Göteborg, Sweden
[c] Volvo Group Trucks Technology, Department of Common Architecture and Shared Technology, Göteborg, Sweden

ARTICLE INFO

ABSTRACT

This paper investigates the energy consequences of determining the energy-optimal velocity profile and torque distribution sequentially versus jointly in a battery electric vehicle (BEV) with two electric motors, one per axle. Three optimization architectures are evaluated: a centralized architecture (CA), a de-centralized architecture (DCA) and a refined de-centralized architecture (r-DCA). CA jointly optimizes the velocity trajectory and torque distribution for minimal energy consumption in a predictive framework, while DCA solves these subproblems hierarchically: velocity trajectory optimization is performed predictively, and torque distribution is computed instantaneously. The joint optimization in CA leads to a reduction in energy consumption of 3.3% at low velocities and 2.2% in an urban city cycle compared to DCA. To mitigate the energy consequences, the objective function in the predictive layer of DCA is augmented with an aggregated power loss map of the powertrain in r-DCA, which achieves energy savings close to CA.

1. Introduction

The urgency to reduce emissions has never been more critical than it is today. To keep the global temperature rise within the limits set by the Paris Agreement, unprecedented changes are required across all sectors. Between 1990 and 2019, greenhouse gas (GHG) emissions from transport increased by 33%, accounting for approximately one quarter of the EU's total GHG emissions in 2019, with passenger cars contributing 43.9% [1]. It is identified that a significant increase in the adoption of electric vehicles is needed to achieve these goals.

Although the battery electric vehicle (BEV) is considerably more energy-efficient than its petrol-powered counterpart, factors such as lower driving range, long charging times, and insufficient charging infrastructure continue to affect BEV public acceptance negatively [2]. Measures that reduce the energy consumption of BEVs are therefore highly desirable. Energy minimization can be pursued through several research fields, including reducing aerodynamic drag [3], optimizing cabin climate control [4], and improving thermal management of electric motors [5] etc. This paper focuses on how BEV energy consumption is influenced by driving behavior, i.e., the vehicle's motion, and by the utilization of available actuators in generating that motion.

In a transport mission, a certain amount of energy is inevitably required to overcome factors such as road grade and air drag. However, the total energy consumption of the vehicle is higher due to additional losses within the drivetrain and friction brakes. The driving style significantly influences energy use, where aggressive driving characterized by harsh acceleration and deceleration increases consumption [6,7], mainly due to losses related to frequent changes in kinetic energy. Drivers have been encouraged to adopt eco-driving, i.e., an energy-efficient driving style, to reduce the energy consumption. However, increased connectivity and autonomy of vehicles allow for algorithms to preview upcoming road segments and plan motion accordingly in an energy-efficient manner.

To increase the range of BEVs, the authors in [8] develop an eco-driving function that is experimentally evaluated in an urban environment, effectively leading to a 14.1% reduction in energy consumption. In [9], a DP-generated velocity profile reduces the energy consumption by 9.8% compared to the profile of the average driver. The authors in [10] show, using DP, that energy-efficient driving for BEVs may result in Pulse-and-Glide (PnG) at high frequencies, which is a well-known eco-driving mechanism for ICE vehicles [11]. The energy consumption is reduced significantly, with greater savings in the lower speed range (< 20 km/h). The PnG strategy is also found in [12], though at lower frequencies since minimizing the longitudinal jerk is part of the objective function of the optimization problem.

Further opportunities to reduce energy consumption emerge with the electrification of vehicles and the integration of multiple actuators within the powertrain. Previously, there was only one actuator to generate the forward motion in a conventional vehicle — the internal combustion engine (ICE). In BEVs, the powertrain commonly consists of multiple actuators, i.e., electric motors, controlling the same degree of freedom. A vehicle with such a powertrain is *overactuated*. In this case, a longitudinal force request, corresponding to a request on forward motion, can be fulfilled by an infinite number of torque distributions between the motors. The redundancy of motors enable the pursuit of secondary objectives, such as reducing the energy consumption, by allocating torque to minimize the power losses in the drivetrain

One of the first studies regarding power-efficient torque distribution for BEVs was put forward by [13], which identified that the common method to penalize actuator effort to improve energy efficiency does not necessarily result in minimal energy consumption, as it does not consider actuator efficiencies. Instead, the objective was reformulated to penalize the instantaneous power consumption of the actuators, successfully leading to less energy consumption while fulfilling the demand on vehicle motion. This study was the spark to a large body of research that now exists on the topic [14–24]. The total torque demand is derived from a reference velocity trajectory [25,26], such as a drive cycle, or decided by a virtual driver [27,28]. Typically, the optimization is instantaneous [27,29–32], i.e., *power* is minimized as opposed to *energy*.

The joint optimization of torque distribution and velocity trajectory can yield further energy savings in overactuated vehicles. For example, [12] demonstrates that the joint optimization for an electric powertrain with two motors reduces the energy consumption by 8.8% compared to a single-motor configuration. In [33], the joint approach is compared to only optimizing the torque distribution between ICE and electric motor in a HEV. By allowing the velocity to deviate by 0.5 m/s from the reference, the electric cost is reduced by 14.77%, compared to strictly following the reference velocity while only optimizing the power split.

Other studies regarding overactuated BEVs address these two sub-problems individually. The authors in [34], for example, divide the problem in an upper layer, finding a velocity profile that minimizes the battery power based on the total torque of the motors, and a lower layer, finding an energy-optimal torque distribution. The layered approach is also applied in [35], where the higher level determining the speed profile penalizes the rate of change of the desired acceleration to improve energy efficiency. Similar to previous work, the torque distribution is addressed in a lower layer. The resulting hierarchical function architecture is beneficial in terms of adaptability and flexibility for the automotive industry. New technologies and manufacturers emerge rapidly, and increased autonomy and connectivity of cars put tremendous demands on automotive manufacturers to reduce development costs related to the control architecture of each new vehicle. If a function could be reused when developing a new vehicle configuration, development costs would be instantly reduced.

The energy consequences of this hierarchical approach has to the knowledge of the authors not yet been assessed. In this work, the simultaneous and sequential optimization of velocity trajectory and torque distribution to minimize energy consumption is assessed for an overactuated BEV. Two optimization architectures are analyzed: a *centralized* architecture (CA), in which velocity profile and torque distribution are optimized over a finite horizon, and a *de-centralized* architecture (DCA), which adopts a hierarchical function architecture where velocity profile is optimized predictively in an upper layer, and torque distribution instantaneously in a lower layer. In DCA, the optimization of velocity trajectory has no information about the motors' efficiencies, only their combined capabilities. A third architecture is proposed to mitigate the energy consequences while maintaining the hierarchical approach: the *refined de-centralized* architecture (r-DCA). The predictive layer is supplied with knowledge about the aggregated efficiency of the powertrain in the shape of an aggregated power loss map. Similar to DCA, the torque distribution is optimized in the lower instantaneous layer.

The architectures are evaluated in straight line driving including three test cases: low-speed, high-speed, and the Artemis Urban Drive Cycle. They are implemented and solved using the CasADi environment in Matlab.

To summarize, the contribution of this work includes:

(1) Quantifying the effect on energy consumption of decoupling the optimization of velocity profile and torque distribution by comparing three different optimization architectures.
(2) Designing a novel, aggregated power loss map of the powertrain based on the optimal torque distribution.
(3) Presenting a method to improve the decoupled problem that provides similar results as the coupled problem of energy-optimal velocity planning and torque distribution.

The following limitations apply:

(1) Only longitudinal dynamics is considered.
(2) Ideal cooling of the motors is assumed, i.e., the power losses are assumed to depend only on motor torque and rotational velocity.
(3) Only the power associated with the powertrain and motion of the vehicle is considered. The power consumed by auxiliary systems such as HVAC and thermal management of the powertrain and battery is neglected.
(4) The only objective considered in the optimization is to reduce energy consumption. Multi-objective optimization including, e.g., travel time and comfort is outside the scope of this paper.
(5) Driving environment is assumed to be known at the start of the transport mission.

The remainder of the paper is structured as follows. Section 2 presents the vehicle and powertrain configuration together with the general optimal control problem for determining an energy-efficient velocity profile. The three optimization architectures are derived in Section 3. Section 4 describes the simulation environment and presents the results, which are then discussed in Section 5 along with the limitations of the study and directions for future work. Finally, the conclusions are summarized in Section 6.

2. Definition of the optimization problem

The simultaneous optimization of velocity trajectory and torque distribution is performed in a predictive optimization framework. It is compared to a hierarchical approach, in which the optimization is decoupled in a predictive layer for the velocity trajectory, and an instantaneous layer for the torque distribution. This section presents the vehicle configuration considered, as well as the general formulation of the optimal control problem used in the predictive optimization. Since the purpose is not real-time implementation but architecture concept evaluation, the optimal control problem is constructed and solved once for a road segment.

2.1. Vehicle and powertrain configuration

The vehicle analyzed in this study is a conventional SUV equipped with two electric motors: an asynchronous motor (ASM) on the front axle and a permanent magnet synchronous motor (PMSM) on the rear axle. The powertrain configuration is shown in Fig. 1. Each motor drives its respective wheels through a single-speed transmission and an open differential.

Fig. 2 shows the combined efficiency of each electric motor and its corresponding inverter. Assuming ideal motor cooling and nominal battery voltage, power losses are considered to be dependent solely on
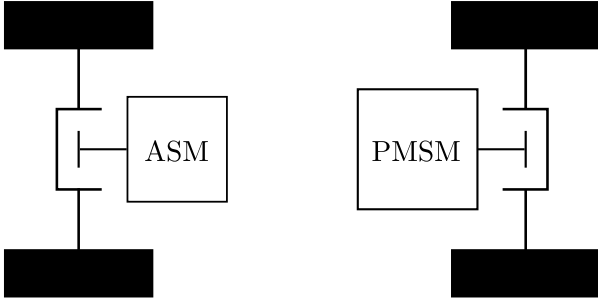
Fig. 1. Powertrain configuration: asynchronous motor (ASM) in the front, permanent magnet synchronous motors (PMSM) in the rear.

Table 1
Vehicle parameters.

Parameter	Description	Value	Unit
m	Vehicle mass	2519	kg
l_f	Distance front axle to CoG	1.523	m
l_r	Distance rear axle to CoG	1.22	m
r_l	Loaded tire radius	0.33	m
n_f	ASM gear ratio	8.55	–
n_r	PMSM gear ratio	9.8	–
C_{rr}	Rolling resistance coefficient	0.02	–
A_f	Frontal area	2.29	m^2
C_d	Aerodynamic drag coefficient	0.32	–
J_{asm}	Rotational inertia ASM	0.073	kg/m^2
J_{pmsm}	Rotational inertia PMSM	0.073	kg/m^2
J_w	Rotational inertia wheel	2.46	kg/m^2

motor torque and rotational speed. These losses are externally supplied using simulations of high-fidelity motor models.

The PMSM offers higher maximum torque and speed and greater efficiency across a wider operating range than the ASM. The braking torque is assumed to be fully provided by the electric motors (100% regenerative braking). The effects of brake-blending strategies on energy consumption are not considered in this study.

The vehicle parameters are shown in Table 1.

2.2. General optimal control problem

The goal of eco-driving is to find (and follow) a velocity profile that minimizes the energy consumed for a given trip. It can be formulated as an optimal control problem with the objective to travel from an initial point s_0 to a final point s_f with minimum energy consumption,

$$\min_{\boldsymbol{x}(s),\boldsymbol{u}(s)} \int_{s_0}^{s_f} F_m(\boldsymbol{x}(s),\boldsymbol{u}(s))ds \tag{1a}$$

$$\text{s. t.} \quad \dot{\boldsymbol{x}}(s) = f(\boldsymbol{x}(s),\boldsymbol{u}(s)) \tag{1b}$$

$$\boldsymbol{x}(s) \in \mathbb{X} \tag{1c}$$

$$\boldsymbol{u}(s) \in \mathbb{U} \tag{1d}$$

where $\boldsymbol{x}(s)$ is a vector containing the state variables, $\boldsymbol{u}(s)$ a vector containing the control variables, $F_m(\cdot)$ is the total force generated by the motors, $f(\cdot)$ describes the dynamics of the state variables, and $\mathbb{X}$ and $\mathbb{U}$ are the feasible sets of the state and control variables respectively. The total force in the objective function can be further divided into two components,

$$F_m(\boldsymbol{x}(s),\boldsymbol{u}(s)) = F_x(\boldsymbol{x}(s),\boldsymbol{u}(s)) + F_{x,loss}(\boldsymbol{x}(s),\boldsymbol{u}(s)) \tag{2}$$

where $F_x(\cdot)$ denotes the longitudinal force contributing to the vehicle's motion, and $F_{x,\text{loss}}(\cdot)$ represents the force equivalent of the power losses in the electric motors. In eco-driving studies for electric vehicles, the electrochemical efficiency of the battery is typically simplified or neglected [10,12,36]. Moreover, modern batteries exhibit lower

internal resistance and higher operating voltage, resulting in improved efficiency. Therefore, battery efficiency is neglected in this work. The term $F_{m,\text{loss}}$ is either included or set to zero in (1), depending on the optimization architecture. Further details are provided in Section 3 where the different architecture concepts are presented.

The state vector is defined as $\boldsymbol{x}(s) = \begin{bmatrix} t(s) & K(s) \end{bmatrix}^T$ where $t(s)$ is time and $K(s) = \frac{v_x(s)^2}{2}$ is kinetic energy normalized by mass. The corresponding state dynamics are given by:

$$\dot{\boldsymbol{x}}(s) = \frac{d\boldsymbol{x}(s)}{ds} = \begin{bmatrix} \frac{1}{\sqrt{2K(s)}} \\ \dot{v}_x(s) \end{bmatrix} \tag{3}$$

A particle model is used according to Fig. 3 with the longitudinal motion of the particle $\dot{v}_x(s)$ (assuming no lateral movement) is given by,

$$\dot{v}_x(s) = \frac{1}{m_s}\left(F_x(s) - F_{air}(s) - F_{rr}(s) - F_g(s)\right) \tag{4}$$

with $F_{air} = \rho_{air}A_f C_d K(s)$, $F_{rr} = mgC_{rr}\cos\phi(s)$ and $F_g = mg\sin\phi(s)$, where ρ_{air} is the air density, A_f the frontal area, C_d the aerodynamic drag coefficient, g the gravitational acceleration, C_{rr} the rolling resistance coefficient, $\phi(s)$ the road slope and m_s the sum of vehicle mass m and equivalent mass of the rotating parts given by,

$$m_s = m + 4\frac{J_w}{r_l^2} + \frac{J_{asm}}{r_l^2}n_f^2 + \frac{J_{pmsm}}{r_l^2}n_r^2 \tag{5}$$

where J_w is the rotational inertia of the wheels, J_{asm} and J_{pmsm} the rotational inertia of the ASM and PMSM, n_f and n_r the front and rear gear ratio respectively. The dependence on s will be dropped from now on for readability.

The feasible set of states, $\mathbb{X}$, is defined by the trip parameters. The kinetic energy is constrained by the velocity limits, $v_{x,\min}$ and $v_{x,\max}$, while time is upper-bounded by the maximum allowable trip duration, t_f. In typical eco-driving studies, time is included in the objective function. The focus of this paper, however, is not to explore the trade-off between time and energy consumption, but rather to quantify the differences in energy consumption between conceptually distinct optimization architectures. Time is therefore deliberately chosen to be loosely constrained, enabling a more flexible exploration of the energy-optimal velocity profile. From a purely energy-efficiency standpoint, the relevant metric is the energy required to travel a given distance. If additional objectives, such as adherence to delivery schedules in freight transport or public transit, are considered, travel time should also be included in the optimization. This is particularly relevant in cases where the cost per time unit (e.g., driver salary) is high relative to the energy cost. The driving scenarios used in this study are described in Section 4.1, where the simulation environment is presented.

Furthermore, the variables in the control vector, $\boldsymbol{u}(s)$, and the corresponding feasible set, $\mathbb{U}$, vary dependent on optimization architecture which will be presented in Section 3.

3. Optimization architecture concepts

Three concepts of optimization architecture are described in this section: a centralized (CA), a de-centralized (DCA) and a refined decentralized (r-DCA) architecture.

Fig. 4 provides an overview of the optimization architectures and the interfaces between their respective layers. The CA architecture is shown at the top of the figure. In CA, the individual motors' power losses are included in the objective function of the OCP (1), and the motor torques serve as the control variables. In contrast, the OCP in DCA, illustrated in the middle of the figure, does not account for motor-related losses when determining the optimal velocity profile. Consequently, only the motion resistance is minimized. The control variable in this case is the total longitudinal force, while the motor torques are optimized for minimum instantaneous power loss in a lower layer, where the optimal longitudinal force from the OCP is
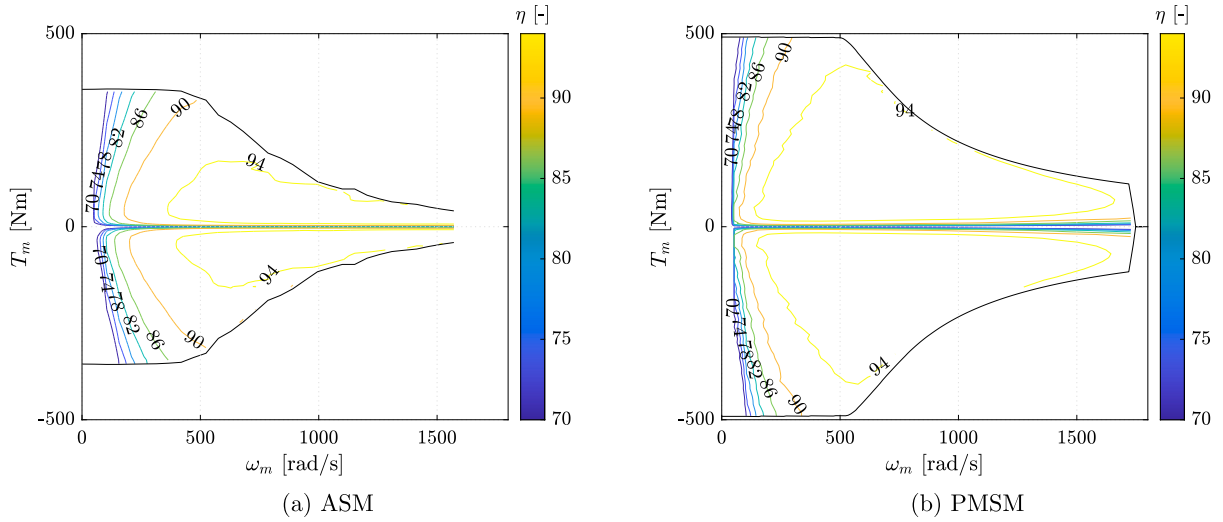
(a) ASM

(b) PMSM

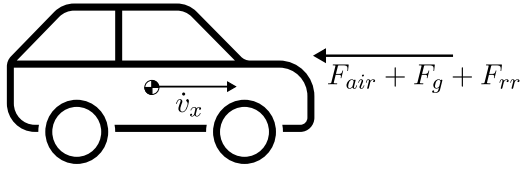**Fig. 2.** Efficiency of the electric motors.

Fig. 3. Particle model with longitudinal dynamics.

implemented as an equality constraint. The architecture for r-DCA is presented at the bottom of the figure. It can be interpreted as a hybrid between CA and DCA: the control variable remains the longitudinal force, but a force loss term associated with motor power losses is included in the objective function. A detailed description of each architecture is provided in the following subsections.

3.1. Centralized optimization architecture (CA)

In CA, the energy-optimal velocity profile and motor torque distribution are found simultaneously in the OCP.

3.1.1. CA optimal control layer

There are two controlled variables; the torque request on the front motor T_{mf} and torque request on the rear motor T_{mr}:

$$\boldsymbol{u}_{CA} = \begin{bmatrix} T_{mf} & T_{mr} \end{bmatrix}^T \tag{6}$$

The feasible set of the motor torques includes operational limits and attainable friction force at the tires. The operational torque limit is dependent on rotational velocity, and is piece-wise fitted with two polynomials to be incorporated as inequality constraints in the OCP,

$$T_{mf,lim1}(\omega_{mf}) = c_{Tf0}\omega_{mf} + c_{Tf1} \tag{7}$$

$$T_{mf,lim2}(\omega_{mf}) = c_{Tf2}\omega_{mf}^3 + c_{Tf3}\omega_{mf}^2 + c_{Tf4}\omega_{mf} + c_{Tf5} \tag{8}$$

$$T_{mr,lim1}(\omega_{mr}) = c_{Tr0}\omega_{mr} + c_{Tr1} \tag{9}$$

$$T_{mr,lim2}(\omega_{mr}) = c_{Tr2}\omega_{mr}^3 + c_{Tr3}\omega_{mr}^2 + c_{Tr4}\omega_{mr} + c_{Tr5} \tag{10}$$

where c_{Tf0}-c_{Tf5} and c_{Tr0}-c_{Tr5} are coefficients of the polynomials for the front and rear motors respectively. The polynomial constraints and corresponding motor data are shown in Fig. 5.

The torque limit based on friction force is derived assuming road-tire friction coefficient $\mu = 1$ and a static normal load for each axle,

$$T_{mf,lim3} = (\mu F_{zf})\frac{r_l}{n_f} \tag{11}$$

$$T_{mr,lim3} = (\mu F_{zr})\frac{r_l}{n_r} \tag{12}$$

where F_{zf}, F_{zr} are the static normal loads for the front and rear axle, and r_l is the loaded wheel radius. The motor torques are limited by the minimum of these three constraints for each axle respectively.

The power losses associated with the motors are included in the objective function. A polynomial approximation of the simulated power loss data, dependent on T_m (propulsive and braking) and ω_m, is obtained using the *cftool* in MATLAB with the linear least-squares method. The polynomial order in both variables is increased until the fitting error is minimized. To improve accuracy in specific regions, particularly around zero torque as low torque demands occur more frequently during everyday driving, selected data points are weighted accordingly. The resulting polynomial expressions are given by,

$$P_{loss,f}(\omega_{mf}, T_{mf}) = \sum_{i=0}^{5}\sum_{j=0}^{4} p_{f,ij}(\omega_{mf})^i(T_{mf})^j \tag{13}$$

$$P_{loss,r}(\omega_{mr}, T_{mr}) = \sum_{i=0}^{5}\sum_{j=0}^{4} p_{r,ij}(\omega_{mr})^i(T_{mr})^j \tag{14}$$

where $p_{f,ij}$ and $p_{r,ij}$ are coefficients of the polynomials for the front and rear motor respectively.

The objective function in (2) is rewritten in terms of the defined state and control variables for CA with,

$$F_x(\boldsymbol{x}, \boldsymbol{u}_{CA}) = (T_{mf}n_f + T_{mr}n_r)\frac{1}{r_l} \tag{15}$$

$$F_{x,loss}(\boldsymbol{x}, \boldsymbol{u}_{CA}) = \frac{1}{\sqrt{2K}}\left(P_{loss,f}\left(\sqrt{2K}\frac{n_f}{r_l}, T_{mf}\right) + P_{loss,r}\left(\sqrt{2K}\frac{n_r}{r_l}, T_{mr}\right)\right) \tag{16}$$

Incorporating the derived constraints and the objective function, the resulting OCP is found.

$$\min_{\boldsymbol{x},\boldsymbol{u}_{CA}} \int_{s_0}^{s_f} \left((T_{mf}n_f + T_{mr}n_r)\frac{1}{r_l} + \right.$$

$$\left. \frac{1}{\sqrt{2K}}\left(P_{loss,f}\left(\sqrt{2K}\frac{n_f}{r_l}, T_{mf}\right) + P_{loss,r}\left(\sqrt{2K}\frac{n_r}{r_l}, T_{mr}\right)\right)\right) ds \tag{17a}$$

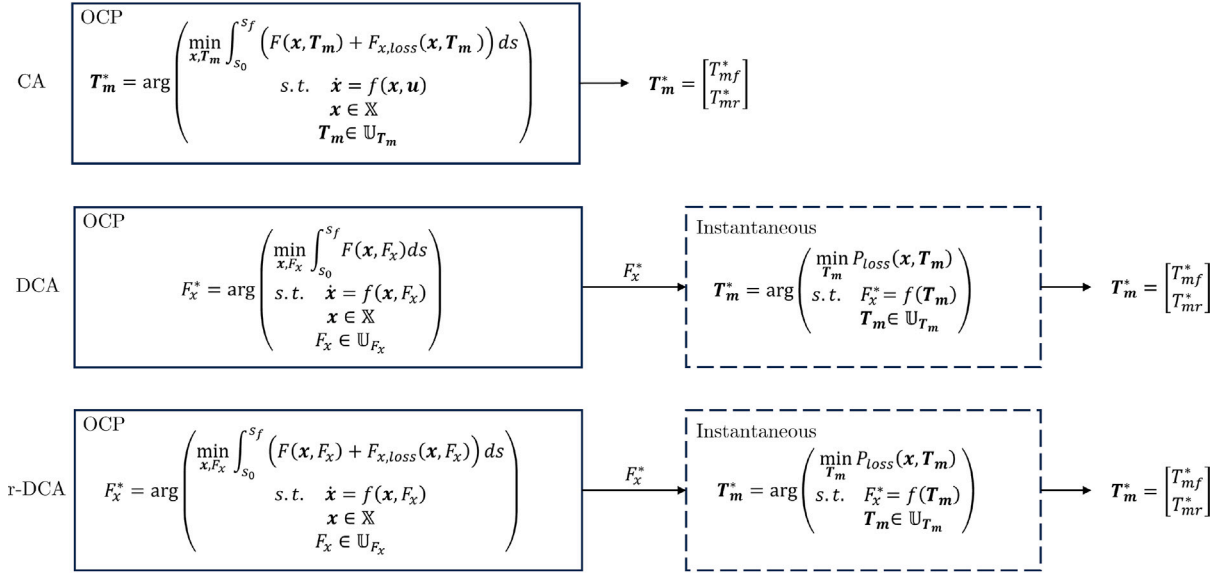$$\text{s.t.} \quad \dot{\boldsymbol{x}} = \begin{bmatrix} \frac{1}{\sqrt{2K}} \\ \dot{v}_x \end{bmatrix} \tag{17b}$$

Fig. 4. Overview of the three optimization architectures; centralized (top), de-centralized (middle) and refined de-centralized (bottom).
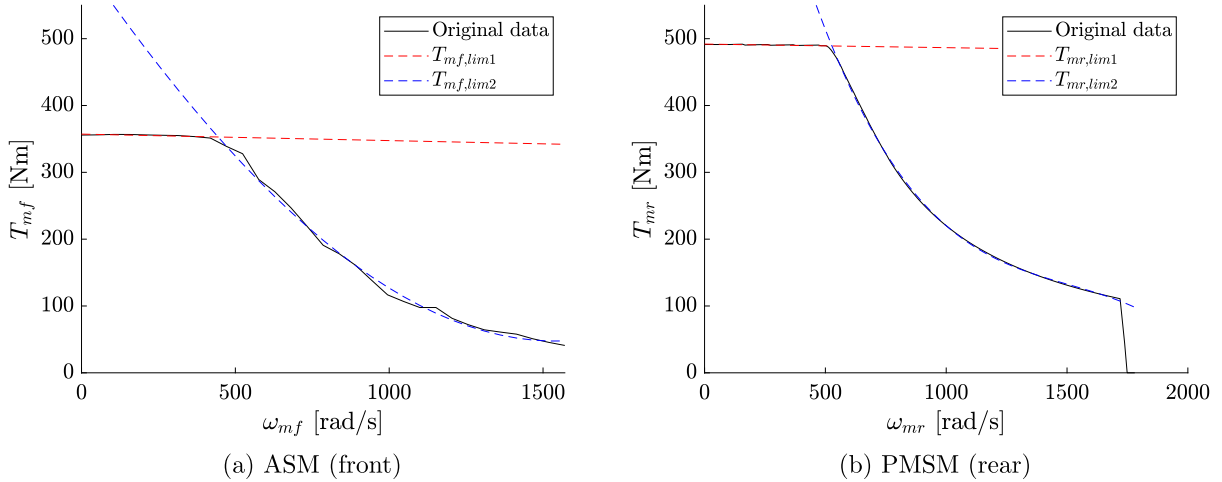

(a) ASM (front)   (b) PMSM (rear)

Fig. 5. Torque capabilities.

$$\dot{v}_x = \frac{1}{m_s}\left((T_{mf}n_f + T_{mr}n_r)\frac{1}{r_l} - \rho_{air}A_f C_d K - mgC_{rr}\cos\phi - mg\sin\phi\right)$$

$$(17c)$$

$$|T_{mf}| - \min\left[T_{mf,lim1}\left(\sqrt{2K}\frac{n_f}{r_l}\right), T_{mf,lim2}\left(\sqrt{2K}\frac{n_f}{r_l}\right), T_{mf,lim3}\right] \le 0$$

$$(17d)$$

$$|T_{mr}| - \min\left[T_{mr,lim1}\left(\sqrt{2K}\frac{n_r}{r_l}\right), T_{mr,lim2}\left(\sqrt{2K}\frac{n_r}{r_l}\right), T_{mr,lim3}\right] \le 0 \quad (17e)$$

$$\frac{1}{2}v_{x,min}^2 \le K \le \frac{1}{2}v_{x,max}^2 \tag{17f}$$

$$K(s_0) - \frac{1}{2}v_{x0}^2 = 0 \tag{17g}$$

$$K(s_f) - \frac{1}{2}v_{xf}^2 = 0 \tag{17h}$$

$$t(s_f) - t_f \le 0 \tag{17i}$$

where v_{x0} and v_{xf} are the initial and final velocity, and t_f the maximum travel time specified in Section 4.1.

3.2. De-centralized optimization architecture (DCA)

DCA consists of an OCP solving for the energy optimal velocity trajectory and longitudinal force request, and a instantaneous layer

solving for the power optimal distribution of motor torque between the ASM and PMSM such that the optimal longitudinal force demand from the OCP is met.

3.2.1. DCA optimal control layer

In DCA, the OCP has only one controlled variable: total longitudinal force F_x,

$$u_{DCA} = \begin{bmatrix} F_x \end{bmatrix} \tag{18}$$

The feasible set of u_{DCA} is defined by the combined capability of the motors given by,

$$F_{x,lim}(v_x) = \frac{1}{r_l}\left(T_{mf,lim}\left(\frac{\omega_{mf}r_l}{n_f}\right)n_f + T_{mr,lim}\left(\frac{\omega_{mr}r_l}{n_r}\right)n_r\right) \tag{19}$$

The longitudinal force limit is piece-wise fitted with two polynomials in the same way as the torque limits in CA,

$$F_{x,lim1}(v_x) = c_{Fx0}v_x + c_{Fx1} \tag{20}$$

$$F_{x,lim2}(v_x) = c_{Fx2}v_x^3 + c_{Fx3}v_x^2 + c_{Fx4}v_x + c_{Fx5} \tag{21}$$

where c_{Fx0}-c_{Fx5} are coefficients of the polynomials. The longitudinal force is also limited by the available friction force. Since F_x is the

total longitudinal force of the vehicle, the total static normal load is considered,

$$F_x \le \mu \left(F_{zf} + F_{zr} \right) \tag{22}$$

Proceeding from the OCP defined in (1), removing $F_{x,loss}$ from the objective function and incorporating limits for F_x, the OCP for DCA is obtained,

$$\min_{x, u_{DCA}} \int_{s_0}^{s_f} F_x \, ds \tag{23a}$$

$$\text{s.t.} \quad \dot{x} = \begin{bmatrix} \frac{1}{\sqrt{2K}} \\ \dot{v}_x \end{bmatrix} \tag{23b}$$

$$\dot{v}_x = \frac{1}{m_s} \left(F_x - \rho_{air} A_f C_d K - mg C_{rr} \cos\phi - mg \sin\phi \right) \tag{23c}$$

$$|F_x| - \min\left[F_{x,lim1}(\sqrt{2K}), F_{x,lim2}(\sqrt{2K}), F_{x,lim3} \right] \le 0 \tag{23d}$$

$$\frac{1}{2} v_{x,min}^2 \le K \le \frac{1}{2} v_{x,max}^2 \tag{23e}$$

$$K(s_0) - \frac{1}{2} v_{x0}^2 = 0 \tag{23f}$$

$$K(s_f) - \frac{1}{2} v_{xf}^2 = 0 \tag{23g}$$

$$t(s_f) - t_f \le 0 \tag{23h}$$

3.2.2. DCA instantaneous optimization layer

In the instantaneous optimization problem, the electric power losses are minimized in every iteration. It is formulated as:

$$\min_{T_{mf}, T_{mr}} \left(P_{loss,f}\left(v_x \frac{n_f}{r_l}, T_{mf} \right) + P_{loss,r}\left(v_x \frac{n_r}{r_l}, T_{mr} \right) \right) \tag{24a}$$

$$\text{s.t.} \quad F_x^* = \frac{1}{r_l} \left(T_{mf} n_f + T_{mr} n_r \right) \tag{24b}$$

$$|T_{mf}| - \min\left[T_{f,lim1}\left(v_x \frac{n_f}{r_l} \right), T_{f,lim2}\left(v_x \frac{n_f}{r_l} \right), T_{f,lim3} \right] \le 0 \tag{24c}$$

$$|T_{mr}| - \min\left[T_{r,lim1}\left(v_x \frac{n_r}{r_l} \right), T_{r,lim2}\left(v_x \frac{n_r}{r_l} \right), T_{r,lim3} \right] \le 0 \tag{24d}$$

The optimal longitudinal force request, F_x^*, from the predictive optimization layer is treated as an equality constraint, and the motor capabilities are represented by inequality constraints defined by (7)–(10) and available friction force (11). The implementation of the instantaneous optimization problem and its interface with the OCP is presented together with the simulation environment in Section 4.1.

3.3. Refined de-centralized optimization architecture (r-DCA)

The objective function of the OCP in DCA is augmented with aggregated power losses of the motors, referred to as an aggregated power loss map (APLM). The requirement on the APLM is that it should be a function of the optimization variables in DCA, as it should not introduce additional variables to the predictive layer.

3.3.1. Generation of the aggregated power loss map (APLM)

The APLM represents power losses of the entire powertrain, consisting of one or more electric motors, from the perspective of longitudinal vehicle operation, effectively serving as the equivalent of an electric motor's operational map but for the complete vehicle. It is defined by the total longitudinal force and forward velocity, F_x and v_x. The APLM exhibits infinite variability due to overactuation. In other words, for each operating point, defined by one combination of F_x and v_x, there are countless possible motor torque distributions, requiring a predefined allocation. To achieve the most power-efficient map, the torque distribution is optimized for each operating point to minimize power losses in the powertrain, and the corresponding losses are recorded. This means that the torque distribution could vary for different operating points in the APLM. The generation of the APLM is performed in the following way for the considered powertrain configuration:

(1) Define the domain dictated by the capabilities of the combined powertrain: $F_x \in [F_{x,min}, F_{x,max}]$ and $v_x \in [0, v_{x,max}]$

$$F_{x,min} = \max\left(\frac{n_f}{r_l} T_{mf,min}, \mu F_{zf0} \right) + \max\left(\frac{n_r}{r_l} T_{mr,min}, \mu F_{zr0} \right)$$

$$F_{x,max} = \min\left(\frac{n_f}{r_l} T_{mf,max}, -\mu F_{zf0} \right) + \min\left(\frac{n_r}{r_l} T_{mr,max}, -\mu F_{zr0} \right)$$

$$v_{x,max} = \min\left(\frac{\omega_{f,max}}{n_f}, \frac{\omega_{r,max}}{n_r} \right) r_l$$

where n_f and n_r represent the front and rear transmission ratios, $T_{mf,min}$ and $T_{mr,min}$ the lower operational torque limit on the front and rear motor, F_{zf0} and F_{zr0} the static normal load on the front and rear axle, $T_{mf,max}$ and $T_{mr,max}$ the upper operational torque limit on the front and rear motor, and $\omega_{f,max}$ and $\omega_{r,max}$ the maximum rotational speed for the front and rear motor, respectively.

(2) Grid the domain into a number of operating points. Here:
$N_{F_x} = 200$
$N_{v_x} = 100$

(3) Step through each operating point, find the optimal torque distribution through optimization and corresponding combined power losses.

if: $F_x > \left(T_{mf,max} n_f + T_{mr,max} n_r \right) \frac{1}{r_l}$ or $F_x < \left(T_{mf,min} n_f + T_{mr,min} n_r \right) \frac{1}{r_l}$
then: Force request exceeds powertrain capabilities. Return NaN.

else: (a) Find optimal torque distribution through the instantaneous optimization problem (24), here formulated as a non-linear program and solved using `fmincon` in Matlab.
(b) Use optimal torque distribution to find the combined powertrain losses through interpolation of the original power loss data for the motors. Store power losses in a look-up table.
(c) Calculate the optimal combined powertrain efficiency, η. Store efficiency in a look-up table.

The corresponding aggregated efficiency map is shown in Fig. 6a and the optimal torque distribution can be seen in Fig. 6b. The efficiency is only used for visualization, while the power losses are used in the objective function of the OCP. The powertrain is most efficient for low to medium longitudinal force requests at 15–40 m/s, and the efficiency decreases quite rapidly for velocities below 15 m/s. The power optimal torque distribution in Fig. 6b is predominantly biased towards the rear motor with 65%–80% of the total torque request. At very high longitudinal force requests, the distribution is closer to equal between the motors.

3.3.2. r-DCA optimal control layer

Similar to DCA, the OCP in r-DCA has only one controlled variable: total longitudinal force F_x,

$$u_{rDCA} = \begin{bmatrix} F_x \end{bmatrix} \tag{25}$$

The aggregated power loss map is fitted with a bivariate polynomial dependent on vehicle velocity and longitudinal force,

$$P_{loss,F_x}(v_x, F_x) = \sum_{i=0}^{5} \sum_{j=0}^{2} h_{ij}(v_x)^i (F_x)^j \tag{26}$$

where h_{ij} are coefficients of the polynomial. The power loss polynomial is added to the objective function in the predictive optimization layer of r-DCA. The OCP is then formulated accordingly,

$$\min_{x, u_{rDCA}} \int_{s_0}^{s_f} \left(F_x + \frac{1}{\sqrt{2K}} P_{loss,F_x}(\sqrt{2K}, F_x) \right) ds \tag{27a}$$

(a) Traction diagram with power efficiency contours

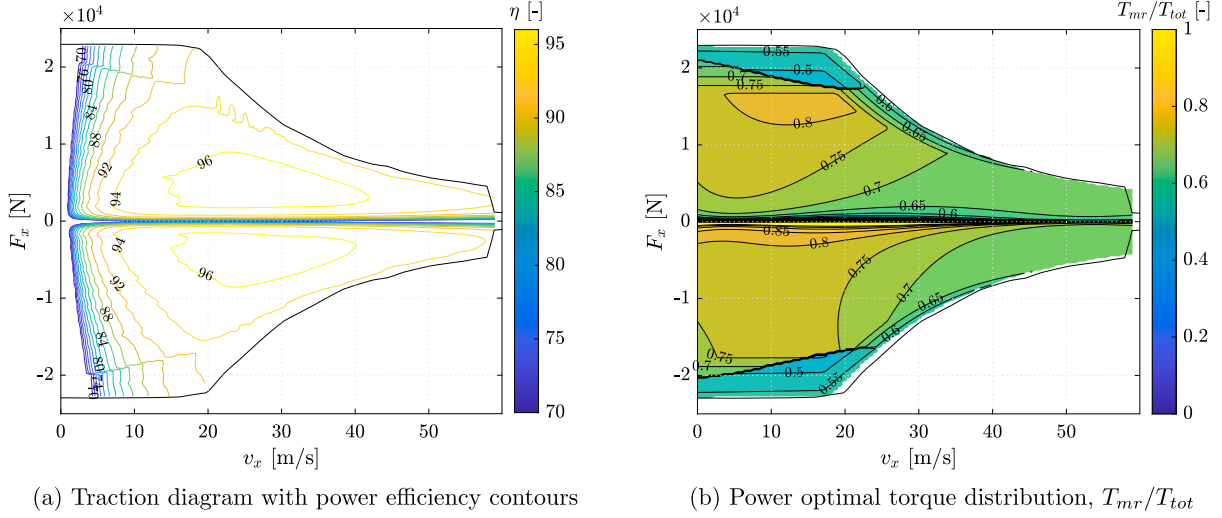(b) Power optimal torque distribution, T_{mr}/T_{tot}

Fig. 6. Powertrain optimal efficiency and distribution.

$$\text{s.t.} \quad \dot{x} = \begin{bmatrix} \frac{1}{\sqrt{2K}} \\ \dot{v}_x \end{bmatrix} \tag{27b}$$

$$|F_x| - \min\left[F_{x,lim1}(\sqrt{2K}), F_{x,lim2}(\sqrt{2K}), F_{x,lim3}\right] \leq 0 \tag{27c}$$

$$\frac{1}{2}v_{x,min}^2 \leq K \leq \frac{1}{2}v_{x,max}^2 \tag{27d}$$

$$K(s_0) - \frac{1}{2}v_{x0}^2 = 0 \tag{27e}$$

$$K(s_f) - \frac{1}{2}v_{xf}^2 = 0 \tag{27f}$$

$$t(s_f) - t_f \leq 0 \tag{27g}$$

3.3.3. r-DCA instantaneous optimization layer

The instantaneous optimization problem is formulated in the same way as for DCA, see (24) in Section 3.2.2.

4. Simulation results in straight driving

Two test cases are considered in this work: a simple case to explore the differences between low- and high-speed driving scenarios, and the Artemis urban drive cycle to evaluate performance in a more dynamic environment.

4.1. Simulation environment

The OCPs defined in previous sections (3.1, 3.2 and 3.3) are implemented in the CasADi [37] environment in Matlab. They are transformed into non-linear programs (NLPs) using multiple-shooting and the Runge–Kutta 4 integrator with four steps per interval and 2500 discretization points N. Road slope is treated as a known constant that changes for every step. The NLPs are then solved using the IPOPT solver.

The resulting optimal control vector (consisting of $[T_{mf}^*, T_{mr}^*]^T$ for CA and $[F_x^*]$ for DCA/r-DCA) for the given segment is forwarded to a first-order particle model with a static powertrain in Matlab Simulink. The particle dynamics is given by,

$$\dot{v}_x = \frac{1}{m_s}\left(\left(T_{mf}n_f + T_{mr}n_r\right)\frac{1}{r_l} - \rho_{air}A_fC_dK - mgC_{rr}\cos\phi - mg\sin\phi\right) \tag{28}$$

A simple model is chosen as opposed to a high fidelity model as it is deemed sufficient for the conceptual study of energy consumption in this paper. For implementation of the derived algorithms, a more refined vehicle dynamics and powertrain model is required to capture possible oscillations and stability issues caused by the redistribution of torque.

For DCA and r-DCA, the instantaneous torque distribution optimization is solved online using the MATLAB function fmincon. Fig. 7 provides an overview of how DCA and r-DCA are integrated into the simulation environment.

The OCP is run offline and provides the optimal control trajectory F_x^* for the prediction horizon N. For each time step $k \in \{1, N\}$, $F_x^*(k)$ in the instantaneous optimization problem is updated and the optimal torque distribution is determined. The resulting front and rear axle torques are then provided to the particle model, which computes the corresponding vehicle velocity v_x and energy consumption using the original power loss data. In the case of CA, the optimal motor torques obtained from the OCP are forwarded directly to the particle model.

4.2. Simple test case

The simple test case consists of a 2500 m road segment with a hill reaching a peak altitude of 40 m at its midpoint. Two speed scenarios are analyzed to represent typical driving conditions: a low-speed case at 15 km/h and a high-speed case at 90 km/h. The purpose of these scenarios is to define representative operating regions and investigate where electric vehicles may benefit from speed planning. The specified velocities are not used as reference trajectories but instead constrain the maximum travel time, t_f, to 600 s for the low-speed case and 100 s for the high-speed case. Consequently, they correspond to two average minimum velocities: $v_{avg,min} = 15$ km/h and $v_{avg,min} = 90$ km/h. The vehicle may therefore complete the segment in less time than t_f. The initial and final velocities, v_0 and v_f, are set to $v_{avg,min}$. The vehicle velocity is further constrained to $v_x \in [1, 200]$ km/h.

4.2.1. Low-speed driving scenario, $v_{avg,min} = 15$ km/h.

The trajectories of velocity, longitudinal force, motor torque, and energy consumption for the low-speed scenario are presented in Fig. 8.

From Fig. 8(a), it can be observed that CA and r-DCA result in increasing velocity profiles, whereas DCA maintains a constant velocity. In the OCP of DCA, the only resistance that can be minimized is the aerodynamic drag, which increases quadratically with velocity. Therefore, the optimal solution is to maintain the lowest possible velocity, limited here by the maximum allowed travel time. When the powertrain losses are included, as in CA and r-DCA, the resulting velocity profile varies according to the combined efficient operating regions of the electric motors.
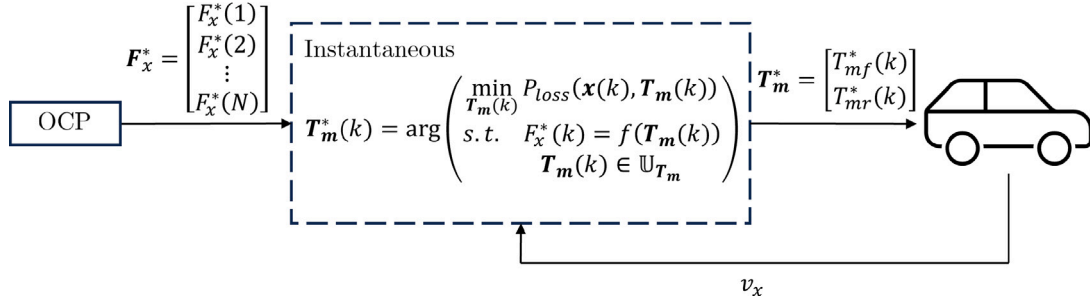
Fig. 7. Simulation environment for DCA and r-DCA.

The influence of road topography on the velocity profile is also evident, with higher velocities before and after the hill and lower velocity at the crest. The longitudinal force, shown in Fig. 8(b), exhibits similar behavior among the architectures, except at the beginning and end of the maneuver, where CA and r-DCA accelerate to and decelerate from higher velocities. Notably, no coasting or PnG events occur where the motor torques are zero. This behavior likely arises because power losses are not assumed to be zero at zero motor torque. As shown in Fig. 8(c), all three architectures allocate more torque to the rear motor, which is expected since the rear PMSM operates more efficiently in this region of the traction diagram (see Fig. 2).

From Fig. 8(d), which illustrates the energy consumption, it can be observed that CA and r-DCA consume more energy than DCA at the beginning of the segment. Around 1250 m, the energy consumption of CA aligns with that of DCA, while r-DCA maintains a higher level throughout most of the distance. Both CA and r-DCA recover more energy at the end of the trip due to regenerative braking.

The trajectories of longitudinal force and velocity in the power-optimal traction diagram are shown in Fig. 8(e), where CA and r-DCA operate in more efficient regions at higher velocities compared to DCA. Examining the power efficiency contours, it is evident that efficiency increases with both velocity and longitudinal force within this operating region. However, higher powertrain efficiency does not necessarily lead to lower overall energy consumption, since the velocity-dependent driving resistances, such as aerodynamic drag, also increase. Thus, increasing velocity to access a higher-efficiency region only reduces total energy consumption if the reduction in power losses outweighs the additional driving resistance.

4.2.2. High-speed driving scenario, $v_{avg,min} = 90$ km/h.

The trajectories of velocity, longitudinal force, motor torque, and energy consumption for the high-speed scenario are presented in Fig. 9.

In Fig. 9(a), it can be observed that DCA again maintains a constant velocity, whereas CA and r-DCA exhibit a sinusoidal-like velocity profile that varies with the road topography. The pattern is similar to that of the low-speed scenario, with the main difference being a smaller velocity variation of approximately ±0.5 m/s from DCA.

As shown in Fig. 9(b), CA and r-DCA generally operate with lower longitudinal force magnitudes, except at the beginning of the maneuver. Similar to the low-speed scenario, the torque distribution is biased towards the rear motor, as seen in Fig. 9(c). Examining the traction diagram in Fig. 9(e), it is less apparent that CA and r-DCA operate in more efficient regions compared to the low-speed scenario. However, efficiency varies primarily with longitudinal force and remains relatively constant with velocity, indicating that increasing velocity provides limited additional benefit in terms of energy efficiency for the powertrain.

Table 2
Time and energy consumption of CA, DCA and r-DCA for the simple test case. Negative numbers indicate a reduction in energy consumption.

$v_{avg,min}$	Strategy	Time [s]	Energy cons., E [kWh]	ΔE
15 km/h	CA	323.8	0.4371	−3.3%
	DCA	600	0.4520	ref
	r-DCA	294.1	0.4390	−2.9%
90 km/h	CA	100	0.5962	−0.1%
	DCA	100	0.5969	ref
	r-DCA	100	0.5962	−0.1%

4.2.3. Energy consumption and time

The final travel time and energy consumption for the two speed scenarios are summarized in Table 2. In the low-speed scenario, CA and r-DCA complete the trip in nearly half the time required by DCA. The energy consumption of CA is reduced by 3.3% compared to DCA, while r-DCA achieves a similar reduction of 2.9%. For the high-speed scenario, the reduction in energy consumption is relatively small, if not negligible, with all three architectures completing the trip in approximately the same time.

4.3. Real world driving cycle: Artemis urban cycle (AUC)

In the simple test case, the velocity was loosely constrained, except for the initial and final velocities. While this flexible setup is useful for exploring energy-efficient velocity profiles, the resulting dynamic profiles for CA and r-DCA, for example, the increased speed in the low-speed scenario, are rarely feasible in practice. To evaluate the effects of decoupling under more realistic conditions, an additional driving scenario is required. For this purpose, the Artemis Urban Cycle (AUC) is employed. The velocity profile defined by this drive cycle serves as the reference velocity, v_{ref}, and the solution is allowed to deviate by up to 10% from it.

$$0.9 \cdot v_{ref} \le v_x \le 1.1 \cdot v_{ref} \tag{29}$$

Furthermore, the lower bound on the reference velocity is set to 10 km/h, as the OCP in its current design cannot handle velocities reaching zero, as in the original AUC.

Fig. 10 presents the velocity profiles of CA, DCA, and r-DCA alongside the reference velocity. The velocity profile of DCA closely follows the lower velocity limit throughout the drive cycle, consistent with the behavior observed in previous scenarios. As in earlier cases, CA and r-DCA exhibit similar velocity profiles, avoiding rapid fluctuations and approaching the upper velocity limit when the reference velocity is low.

The energy consumption results are summarized in Table 3. CA consumes 2.2% less energy than DCA, while r-DCA achieves approximately the same energy efficiency as CA. Following the reference velocity profile of the AUC, $v_x = v_{ref}$, increases energy consumption by 2.0%. Again, DCA requires the longest time to complete the cycle.
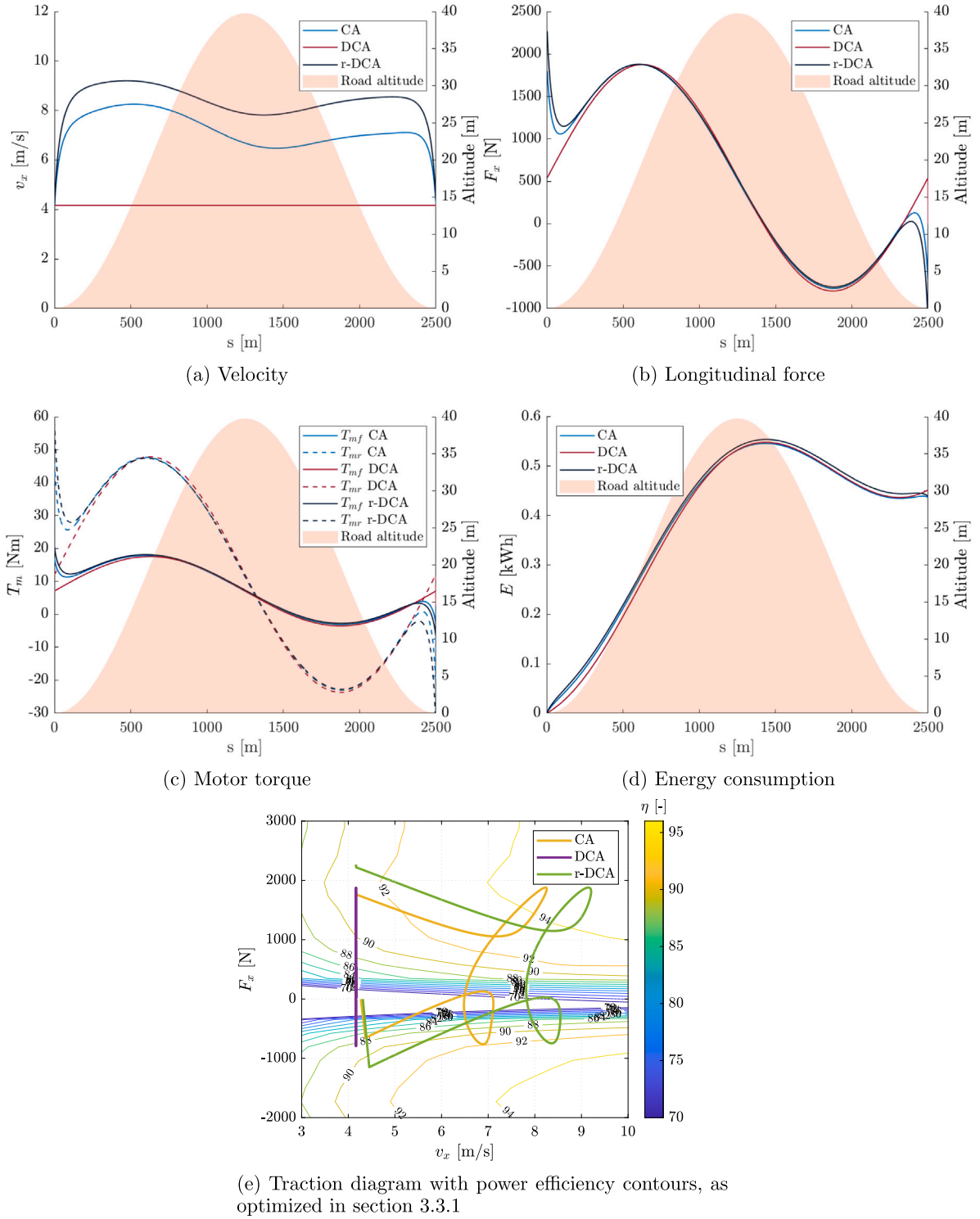
(a) Velocity

(b) Longitudinal force

(c) Motor torque

(d) Energy consumption

(e) Traction diagram with power efficiency contours, as optimized in section 3.3.1
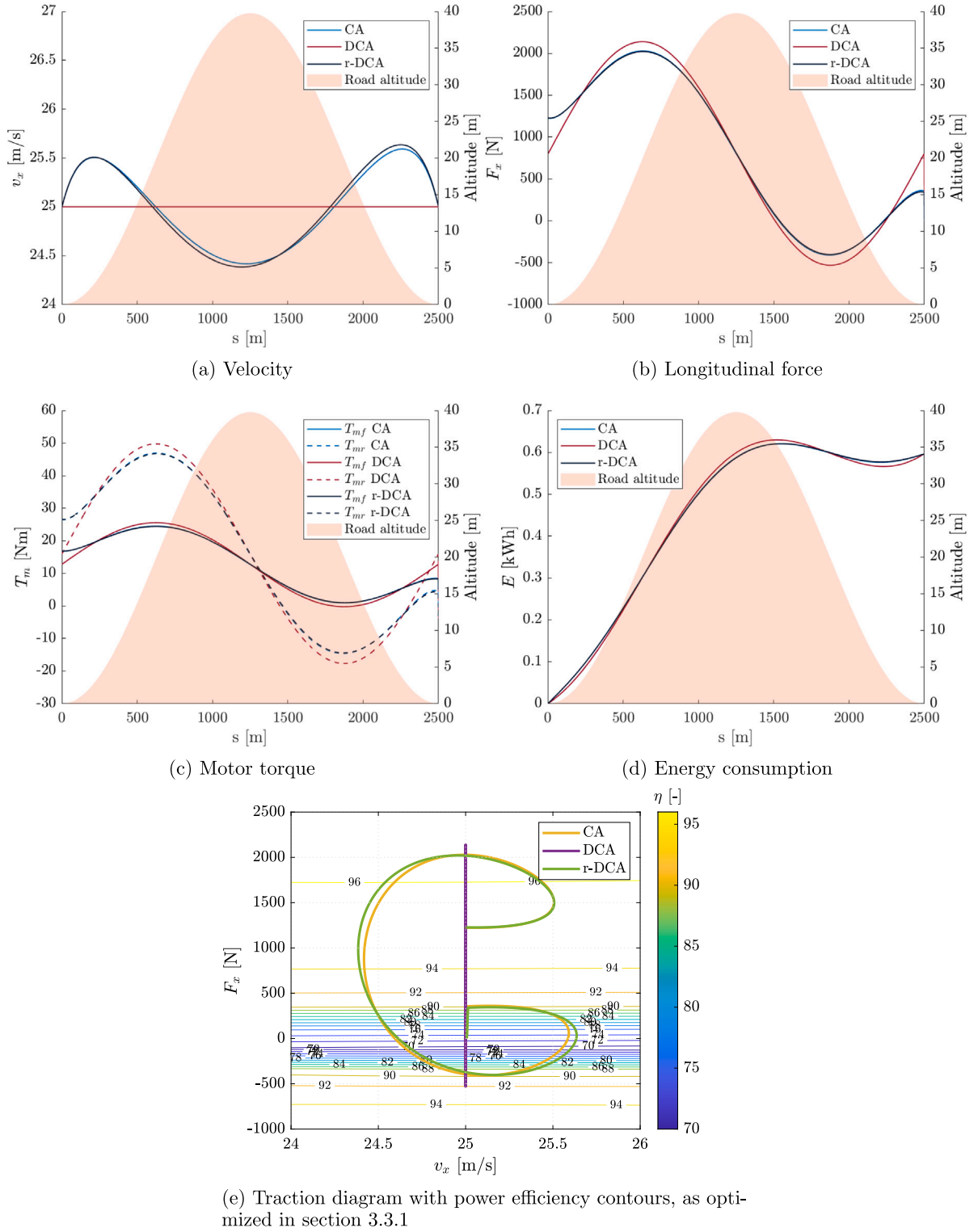
Fig. 8. Results from $v_{avg,min}$ = 15 km/h.

5. Discussion and future work

5.1. Discussion of results

The results presented in Table 2 indicate that including both the velocity profile and torque distribution in the OCP, as in CA, reduces energy consumption by 3.3% for low-speed driving but only by 0.1% for high-speed driving. Examining the efficiency contours in Fig. 2 reveals that efficiency varies primarily with velocity in the low-speed region

and with longitudinal force in the high-speed region. Consequently, varying the velocity profile at higher speeds provides little additional benefit in terms of energy consumption.

Interestingly, CA and r-DCA adopt higher velocities in the low-speed scenario, which contradicts the common eco-driving guideline of maintaining a low and constant speed. The OCPs in CA and r-DCA predict that the reduction in motor power losses outweighs the increase in aerodynamic drag, leading to increased velocities. However, achieving the full 3.3% energy reduction requires a velocity increase of

(a) Velocity

(b) Longitudinal force

(c) Motor torque

(d) Energy consumption

(e) Traction diagram with power efficiency contours, as optimized in section 3.3.1

Fig. 9. Results from $v_{avg,min}$ = 90 km/h.

4–5 m/s, approximately twice the initial and final speed, an increase that may be unrealistic in practical low-speed scenarios such as city driving. In this study, such deviations are considered acceptable since the primary objective is to evaluate different optimization architectures in terms of energy consumption rather than to develop an immediately implementable control strategy. Nevertheless, a rapid increase in velocity could potentially cause discomfort for vehicle occupants. From the longitudinal force shown in Fig. 9(b), and using the vehicle mass

specified in Table 1, the corresponding longitudinal acceleration can be estimated to approximately 1 m/s^2, which is well within a comfortable range for passengers. In addition, the maximum longitudinal jerk produced by any of the three architectures is approximately 0.02 m/s^3, which is well below the comfort threshold [38].

Furthermore, the travel time for CA and r-DCA is significantly shorter than for DCA, which could raise concerns about the fairness of the comparison. As noted earlier, the objective of this paper is to
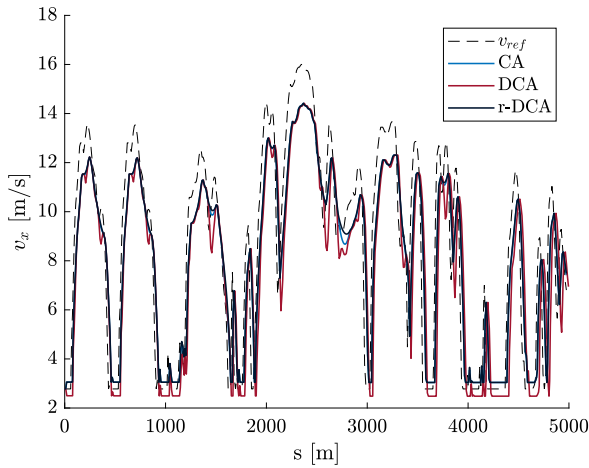
Fig. 10. Velocity profiles for Artemis urban drive cycle: reference, CA, DCA, and r-DCA.

Table 3
Energy consumption of CA, DCA and r-DCA for the Artemis Urban City Cycle. Negative numbers indicate a reduction in energy consumption.

v_{ref} [km/h]	Strategy	Time [s]	E [kWh]	ΔE
AUC	$v_x = v_{ref}$	813.2	0.9668	2.0%
	CA	802.3	0.9267	−2.2%
	DCA	903.3	0.9472	ref
	r-DCA	798.8	0.9268	−2.2%

quantify the differences in energy consumption between the three optimization architectures. To minimize restrictions on the solution, travel time is not penalized in the objective function but is only constrained by a maximum value. The comparison remains fair because all three architectures share the same boundary conditions and state constraints. Notably, the results show that energy consumption can be reduced by 3.3% while completing the trip in approximately half the time, which contradicts the common assumption that lower velocities always yield lower energy consumption.

By refining DCA with an aggregated powertrain efficiency map, as in r-DCA, energy consumption is reduced by approximately 2.9% compared to DCA. This demonstrates that the OCP for determining an energy-optimal velocity profile and torque distribution can be divided into two separate optimization problems, provided that aggregated information about the powertrain efficiency is available in the velocity planning layer. Consequently, the number of optimization variables in the OCP is reduced, as the torque distribution between the motors is not handled in this layer but instead represented by a single total longitudinal force request. In other words, the number of controlled variables in the OCP is decreased, which could lower the computational effort. The instantaneous optimization in r-DCA could be considered redundant, as the torque distribution has already been optimized to generate the aggregated power loss map. A lookup table dependent on longitudinal force and velocity could therefore be used instead, simplifying implementation in a real vehicle.

5.2. Limitations and future work

The work presented in this paper has analyzed the separation of velocity trajectory optimization and torque distribution within a limited scope. Several factors remain to be explored to extend this analysis. One such factor is the inclusion of lateral dynamics. Road curvature imposes an upper bound on velocity to maintain vehicle stability and occupant comfort, which is not captured when only longitudinal dynamics are considered. Additionally, the preferred torque distribution on which

the aggregated power loss map is based may not be feasible in practice due to stability issues caused by combined slip. This could be addressed by augmenting the map with information on road curvature or lateral acceleration. Furthermore, future work should include sensitivity analyses to assess the effects of varying vehicle load, different topography profiles, alternative electric motor types, and other relevant parameters on the overall energy savings of the different architectures.

The possibility of electrically switching off the ASM or mechanically disconnecting the PMSM from the wheels has not been investigated in this work. Including this option could potentially enable PnG operation, as observed in other studies on electric vehicles [10,12]. In the present study, the electric motors are not assumed to have zero losses at zero torque or speed, meaning that allowing the motors to rotate with the wheels without providing torque (i.e., coasting) is not 'free' in terms of energy. Representing the option to connect or disconnect the motors would require integer decision variables in the optimization problem, which significantly increases the computational complexity of solving the OCP efficiently.

A simple simulation model is used instead of a high-fidelity model because the current study does not involve fast dynamics. While pitch and roll dynamics, as well as load transfer, are important for comfort and stability, they have little effect on energy consumption in passenger vehicles. Powertrain dynamics, however, are critical for implementing torque distribution algorithms, as rapid redistribution of torque can induce oscillations in the powertrain that may compromise comfort and stability. The interaction with existing stability systems must also be considered. In situations where vehicle stability is threatened, energy efficiency is no longer the primary objective; instead, a transition from the energy-efficient algorithm to the stability system could occur when thresholds for yaw rate or vehicle sideslip are exceeded.

Finally, the derived algorithms are not intended for real-time vehicle implementation. The control strategy employed is open-loop, meaning that no feedback from the vehicle is used to verify whether the target velocity is achieved through the applied torque requests. Future work should investigate real-time implementation methods, such as model predictive control, which incorporate closed-loop feedback. Although the algorithms are not optimized for computational efficiency, notable differences in computation time were observed during the Artemis Urban Cycle. Specifically, DCA and r-DCA were more than twice as fast as CA (CA: 22.875 s, DCA: 2.267 s, r-DCA: 8.667 s), measured on a standard laptop equipped with an Intel i7 3.00 GHz processor. To accurately assess computational effort, the algorithms should first be optimized for convergence and then compared under consistent conditions.

6. Conclusions

The aim of this work was to evaluate the impact of separating velocity trajectory optimization and motor torque distribution into two smaller optimization problems on energy consumption in electric vehicles. Specifically, the study focused on whether torque distribution can be managed instantaneously without compromising the potential for reducing total energy consumption.

Three optimization architectures are presented: a centralized (CA), a de-centralized (DCA), and a refined de-centralized architecture (r-DCA). In the centralized architecture, a single optimal control problem is formulated that simultaneously optimizes both the velocity profile and motor torque distribution. The objective function includes total energy consumption, accounting for losses in the electric motors. In the de-centralized architecture, the optimal control problem optimizes only the velocity profile, without incorporating powertrain efficiency in the objective function. Instead, motor power losses are minimized instantaneously while satisfying the resulting longitudinal force corresponding to the optimal velocity profile. In the refined de-centralized architecture, a novel aggregated power loss map of the electric motors

is derived and incorporated into the objective function, while torque distribution is still optimized instantaneously.

The three architectures were evaluated in a simple test case with varying topography at low and high speeds, as well as in the Artemis Urban City Cycle (AUC), representing a more realistic driving scenario. Comparing the centralized and de-centralized architectures, it was found that simultaneously optimizing the velocity trajectory and torque distribution reduces energy consumption by 3.3% in the low-speed scenario, compared to optimizing the two tasks sequentially. The refined de-centralized architecture further reduces energy consumption by 2.9% relative to the de-centralized architecture. For the high-speed scenario, the difference in energy consumption between the architectures was very small, if not negligible. In the AUC, both the centralized and refined de-centralized architectures reduce energy consumption by 2.2% compared to the de-centralized architecture. These results indicate that separating the optimization of velocity profile and motor torque distribution has minimal impact on potential energy savings, provided that the objective function in the optimal control problem incorporates aggregated power loss information for the powertrain.

CRediT authorship contribution statement

Juliette Torinsson: Writing – original draft, Visualization, Software, Methodology, Investigation, Formal analysis, Data curation, Conceptualization. **Mats Jonasson:** Writing – review & editing, Supervision, Conceptualization. **Derong Yang:** Writing – review & editing, Supervision. **Bengt Jacobson:** Writing – review & editing, Supervision, Project administration. **Toheed Ghandriz:** Writing – review & editing, Supervision.

Declaration of Generative AI and AI-assisted technologies in the writing process

During the preparation of this work the authors used ChatGPT in order to improve readability and language. After using this tool, the authors reviewed and edited the content as needed and take full responsibility for the content of the publication.

Declaration of competing interest

The authors declare the following financial interests/personal relationships which may be considered as potential competing interests: Juliette Torinsson reports financial support was provided by Swedish Energy Agency. Mats Jonasson reports financial support was provided by Swedish Energy Agency. Derong Yang reports financial support was provided by Swedish Energy Agency. Bengt Jacobson reports financial support was provided by Swedish Energy Agency. Juliette Torinsson reports a relationship with Volvo Car Corporation that includes: employment. Derong Yang reports a relationship with Volvo Car Corporation that includes: employment. Toheed Ghandriz reports a relationship with Volvo Group Truck Technology that includes: employment. Juliette Torinsson has patent Energy efficient speed recommendation based on lumped powertrain efficiency for electric vehicles pending to Volvo Car Corporation. Derong Yang has patent Energy efficient speed recommendation based on lumped powertrain efficiency for electric vehicles pending to Volvo Car Corporation. Mats Jonasson has patent Energy efficient speed recommendation based on lumped powertrain efficiency for electric vehicles pending to Volvo Car Corporation. If there are other authors, they declare that they have no known competing financial interests or personal relationships that could have appeared to influence the work reported in this paper.

Acknowledgments

Data availability

The authors do not have permission to share data.

References

[1] European Environment Agency, Transport and environment report 2022 - digitalisation in the mobility system: challenges and opportunities, Eur. Environ. Agency (07/2022) (2022) Available: https://www.eea.europa.eu/en/analysis/publications/transport-and-environment-report-2022. (Accessed 14 January 2024).

[2] M. Wicki, G. Brückmann, F. Quoss, T. Bernauer, What do we really know about the acceptance of battery electric vehicles? - turns out, not much, Transp. Rev. 43 (1) (2023) 62–87, http://dx.doi.org/10.1080/01441647.2021.2023693.

[3] M. Urquhart, M. Varney, S. Sebben, M. Passmore, Aerodynamic drag improvements on a square-back vehicle at yaw using a tapered cavity and asymmetric flaps, Int. J. Heat Fluid Flow 86 (2020) http://dx.doi.org/10.1016/j.ijheatfluidflow.2020.108737.

[4] A. Ramesh Babu, S. Sebben, Z. Chronéer, S. Etemad, An adaptive cabin air recirculation strategy for an electric truck using a coupled CFD-thermoregulation approach, Int. J. Heat Mass Transfer 221 (2024).

[5] X. Wang, B. Li, D. Gerada, K. Huang, I. Stone, S. Worrall, Y. Yan, A critical review on thermal management technologies for motors in electric cars, Appl. Therm. Eng. 201 (2022) http://dx.doi.org/10.1016/j.applthermaleng.2021.117758, part A.

[6] C. Bingham, C. Walsh, S. Carroll, Impact of driving characteristics on electric vehicle energy consumption and range, IET Intell. Transp. Syst. 6 (2012) http://dx.doi.org/10.1049/iet-its.2010.0137.

[7] M. Jafari, A. Gauchia, K. Zhang, L. Gauchia, Simulation and analysis of the effect of real-world driving styles in an EV battery performance and aging, IEEE Trans. Transp. Electrification 4 (1) (2015) http://dx.doi.org/10.1109/TTE.2015.2483591.

[8] W. Dib, A. Chasse, P. Moulin, A. Sciarretta, G. Corde, Optimal energy management for an electric vehicle in eco-driving applications, Control Eng. Pract. 29 (2014) 299–307, http://dx.doi.org/10.1016/j.conengprac.2014.01.005.

[9] D. Lu, M. Ouyang, J. Gu, J. Li, Optimal velocity control for a battery electric vehicle driven by permanent magnet synchronous motors, Math. Probl. Eng. (2014) http://dx.doi.org/10.1155/2014/193960.

[10] K.M. So, P. Gruber, D. Tavernini, A.E.H. Karci, A. Sorniotti, T. Motaln, On the optimal speed profile for electric vehicles, IEEE Access 8 (2020) 78504–78518, http://dx.doi.org/10.1109/ACCESS.2020.2982930.

[11] A. Sciarretta, A. Vahidi, Energy-efficient driving of road vehicles, toward cooperative, connected, and automated mobility, in: Lecture Notes in Intelligent Transportation and Infrastructure, Springer, 2020, http://dx.doi.org/10.1007/978-3-030-24127-8.

[12] A. Koch, T. Bürchner, T. Herrmann, M. Lienkamp, Eco-driving for different electric powertrain topologies considering motor efficiency, World Electr. Veh. J. 12 (6) (2021) http://dx.doi.org/10.3390/wevj12010006.

[13] Y. Chen, J. Wang, Energy-efficient control allocation for over-actuated systems with electric vehicle applications, DSCC2010, in: ASME 2010 Dynamic Systems and Control Conference, vol. 1, 2010, http://dx.doi.org/10.1115/DSCC2010-4012.

[14] J. Gu, M. Ouyang, D. Lu, J. Li, L. Lu, Energy efficiency optimization of electric vehicle driven by in-wheel motors, Int. J. Automot. Technol. 14 (2013) http://dx.doi.org/10.1007/s12239-013-0084-1.

[15] Z. Song, H. Hofmann, J. Li, Y. Wang, D. Lu, M. Ouyang, J. Du, Torque distribution strategy for multi-PMSM applications and optimal acceleration control for four-wheel-drive electric vehicles, J. Dyn. Syst. Meas. Control. Trans. the ASME 142 (2020) http://dx.doi.org/10.1115/1.4045321.

[16] A. Pennycott, L. De Novellis, A. Sabbatini, P. Gruber, A. Sorniotti, Reducing the motor power losses of a four-wheel drive, fully electric vehicle via wheel torque allocation, Proc. Inst. Mech. Eng. Part D: J. Automob. Eng. 228 (2014) http://dx.doi.org/10.1177/0954407013516106.

[17] L. De Novellis, A. Sorniotti, P. Gruber, Driving modes for designing the cornering response of fully electric vehicles with multiple motors, Mech. Syst. Signal Process. (2015) 64–65, http://dx.doi.org/10.1016/j.ymssp.2015.03.024.

[18] L. De Novellis, A. Sorniotti, P. Gruber, Optimal wheel torque distribution for a four-wheel-drive fully electric vehicle, SAE Int. J. Passeng. Cars - Mech. Syst. 6 (2013) doi: 10.4271/2013-01-0673.

[19] X. Wu, D. Zheng, T. Wang, J. Du, Torque optimal allocation strategy of all-wheel drive electric vehicle based on difference of efficiency characteristics between axis motors, Energies 12 (2019) http://dx.doi.org/10.3390/en12061122.

[20] L. De Novellis, A. Sorniotti, P. Gruber, Wheel torque distribution criteria for electric vehicles with torque-vectoring differentials, IEEE Trans. Veh. Technol. 63 (2014) http://dx.doi.org/10.1109/TVT.2013.2289371.

[21] C. Chatzikomis, M. Zanchetta, P. Gruber, A. Sorniotti, B. Modic, T. Motaln, L. Blagotinsek, G. Gotovac, An energy-efficient torque-vectoring algorithm for electric vehicles with multiple motors, Mech. Syst. Signal Process. 128 (2019) http://dx.doi.org/10.1016/j.ymssp.2019.03.012.

[22] G. Li, W. Zhuang, Y. Ren, G. Yin, Y. Ding, Energy-oriented torque allocation strategy design of 4wid electric vehicle using slope information, in: SAE Technical Papers, 2019, http://dx.doi.org/10.4271/2019-01-0461.

[23] X. Zhang, D. Göhlich, Optimal torque distribution strategy for a four motorized wheels electric vehicle, EVS, in: 28th International Electric Vehicle Symposium and Exhibition, vol. 2015, (2015) 2015.

[24] Y. Chen, J. Wang, Adaptive energy-efficient control allocation for planar motion control of over-actuated electric ground vehicles, vol. 22, 2014, http://dx.doi.org/10.1109/TCST.2013.2287560.

[25] Y. Chen, J. Wang, Energy-efficient control allocation with applications on planar motion control of electric ground vehicles, in: Proceedings of the 2011 American Control Conference, San Francisco, CA, USA, 2011, pp. 2719–2724, http://dx.doi.org/10.1109/ACC.2011.5991160.

[26] H. Fujimoto, S. Harada, Model-based range extension control system for electric vehicles with front and rear driving-braking force distributions, IEEE Trans. Ind. Electron. 65 (5) (2015) 3245–3254, http://dx.doi.org/10.3390/en12061122.

[27] J. Torinsson, M. Jonasson, D. Yang, B. Jacobson, Energy reduction by power loss minimisation through wheel torque allocation in electric vehicles: a simulation-based approach, Veh. Syst. Dyn. 60 (5) (2020) 1488–1511, http://dx.doi.org/10.1080/00423114.2020.1858121.

[28] B. Li, A. Goodarzi, A. Khajepour, S. Chen, B. Litkouhi, An optimal torque distribution control strategy for four-independent wheel drive electric vehicles, Veh. Syst. Dyn. 53 (8) (2015) 1172–1189, http://dx.doi.org/10.1080/00423114.2015.1028414.

[29] A.M. Dizqah, B. Lenzo, A. Sorniotti, P. Gruber, S. Fallah, J. De Smet, A fast and parametric torque distribution strategy for four-wheel-drive energy-efficient electric vehicles, IEEE Trans. Ind. Electron. 63 (7) (2016) 4367–4376, http://dx.doi.org/10.1109/TIE.2016.2540584.

[30] G. De Filippis, B. Lenzo, A. Sorniotti, P. Gruber, W. De Nijs, Energy-efficient torque-vectoring control of electric vehicles with multiple drivetrains, IEEE Trans. Veh. Technol. 67 (6) (2018) 4702–4715, http://dx.doi.org/10.1109/TVT.2018.2808186.

[31] X. Yuan, J. Wang, Torque distribution strategy for a front- and rear-wheel-driven electric vehicle, IEEE Trans. Veh. Technol. 61 (8) (2012) 3365–3374, http://dx.doi.org/10.1109/TVT.2012.2213282.

[32] B. Lenzo, G. De Filippis, A.M. Dizqah, A. Sorniotti, P. Gruber, S. Fallah, W. De Nijs, Torque distribution strategies for energy-efficient electric vehicles with multiple drivetrains, ASME J. Dyn. Syst. Meas. Control. 139 (12) (2017) 121004, http://dx.doi.org/10.1115/1.4037003.

[33] Y. Liu, Z. Huang, J. Li, M. Ye, Y. Zhang, Z. Chen, Cooperative optimization of velocity planning and energy management for connected plug-in hybrid electric vehicles, Appl. Math. Model. 95 (2021) http://dx.doi.org/10.1016/j.apm.2021.02.033.

[34] W. Zhuang, L. Qu, S. Xu, B. Li, N. Chen, G. Yin, Integrated energy-oriented cruising control of electric vehicle on highway with varying slopes considering battery aging, Sci. China Technol. Sci. 63 (2020) 155–165, http://dx.doi.org/10.1007/s11431-019-9559-2.

[35] D. Xia, B. Li, J. Zhang, B. Zhang, N. Zhang, Ecological cooperative adaptive cruise control of over-actuated electric vehicles with in-wheel motor in traffic flow, IET Intell. Transp. Syst. 15 (2021) http://dx.doi.org/10.1049/itr2.12059.

[36] J. Han, A. Sciarretta, L.L. Ojeda, G. De Nunzio, L. Thibault, Safe- and eco-driving control for connected and automated electric vehicles using analytical state-constrained optimal solution, IEEE Trans. Intell. Veh. 3 (2) (2018) 163–172, http://dx.doi.org/10.1109/TIV.2018.2804162.

[37] J.A.E. Andersson, J. Gillis, G. Horn, J.B. Rawlings, M. Diehl, CasADi - a software framework for nonlinear optimization and optimal control, Math. Program. Comput. 11 (2019) http://dx.doi.org/10.1007/s12532-018-0139-4.

[38] K. Czarnecki, Automated driving system (ADS) high-level quality requirements analysis - driving behavior comfort, 2018, http://dx.doi.org/10.13140/RG.2.2.19925.32483.